

Chapter 5

Contact models in multimodal environments

An important finding from the studies in ecological psychology [100, 152] is that listening subjects often tend to describe sounds in terms of causing events; Gaver [59] refers to this attitude as “everyday listening”. According to these studies, the physical properties involved in sound generation can be grouped into two broad categories: *structural invariants* specify individual properties of objects such as size, shape, material. *Transformational invariants* characterize interactions between objects (e.g. collisions, frictions, and so on).

These experimental results can provide significant help in the development of sound models. The problem of sound-source determination is a fundamental question for the sonification of Virtual Environments and for the design of auditory icons [58]. An example application is that of simulated contact with objects in a Virtual Environment. This topic has already been discussed in Sec. 1.4, here it is enough to recall that previous research (see for e.g. [78]) have used signal models based on additive synthesis techniques. Physical models can be advantageous in that they can be easily synchronized with analogous graphic models, thus providing a high degree of coherence and consistency for the perception of objects and events [134]. Moreover, a description of synthesis algorithms in terms of physical generating phenomena can in principle help in conveying structural and transformational invariants in the synthesized sounds. Recent works [104, 54, 105, 107] have shown that oversimplified physical models are able to convey information on structural invariants related to geometrical properties of the resonators (such as shape and size) and to synthesize “cartoon” sounding objects where these invariants can be controlled. This chapter presents results about a third structural invariant, i.e. *material*, and about a structural invariant, namely *collision*.

A physical model is developed in Sec. 5.1, where a non-linear contact force excites a lumped resonator, and issues related to numerical implementation are discussed. The basic properties of the model are then investigated both analytically and experimentally in Sec. 5.2. Due to the simple structure of the system, it is possible to study the influence

This chapter is partially based on [12, 14, 108].

quantity	symbol	unit
No. of oscillators	N	
Oscill. positions	x_{ol} ($l = 1 \dots N$)	[m]
Oscill. velocities	\dot{x}_{ol} ($l = 1 \dots N$)	[m/s]
Hammer position	x_h	[m]
Hammer velocity	\dot{x}_h	[m/s]
Penetration	$x = x_h - \sum_{l=1}^N x_{ol}$	[m]
Penetration velocity	$\dot{x} = \dot{x}_h - \sum_{l=1}^N \dot{x}_{ol}$	[m/s]
Oscill. masses	m_o	[Kg]
Oscill. center freqs.	ω_{ol}	[rad]
Oscill. quality factor	q_o	
Oscill. damping coeffs.	$g_{ol} = \omega_{ol}/q_o$	[rad]
Hammer mass	m_h	[Kg]
Non-linear exponent	$\alpha = 2.8$	
Elastic constant	k	[N/m $^\alpha$]
Damping weight	λ	[Ns/m $^{\alpha+1}$]
Viscoel. charact.	$\mu = \lambda/k$	[s/m]

Table 5.1: *Symbols used throughout the chapter.*

of physical parameters (hammer and resonator masses, elasticity and damping coefficients of the non-linear contact force) on the system behavior. Contact time, in particular, can be an important cue for the perception of collision. Finally, Sec. 5.3 discusses the ability of the model to convey perception of material to the listener.

Although performed using elementary resonator models, this investigation can also be helpful for improving existing contact models in more complex systems: one example is hammer-string interaction in piano models, where contact time is a key feature for sound quality. The Stulov model [133] for piano hammer felts provides a realistic description of hysteretic contact forces, and is successful in fitting real data. However, recent research by Giordano and Mills [65] has questioned to some extent its general validity, suggesting the need for further investigations on alternative piano hammer models.

5.1 A hammer-resonator model

This section introduces a contact model made of two main blocks, namely a lumped hammer and a lumped resonator. The two blocks interact through a non-linear contact force. The contact force and its main properties are reviewed in Sec. 5.1.1. The interaction with a basic resonator model is discussed in Sec. 5.1.2, and details of the numerical implementation are discussed. Table 5.1 summarizes the main variables and parameters used throughout the chapter.

5.1.1 Non-linear contact force

Contact force models for collisions have been widely studied in musical acoustics, mainly in relation with hammer models in the piano. Assuming that the contact geometry is small (ideally, a point), an idealized model [66] states a polynomial dependence of the force f on the penetration x :

$$f(x(t)) = \begin{cases} -k[x(t)]^\alpha, & x > 0, \\ 0, & x \leq 0, \end{cases} \quad (5.1)$$

where the exponent α depends on the local geometry around the contact surface. As an example, in an ideal impact between two spherical object α takes the value 1.5. Typical values in a piano hammer felt range from 1.5 to 3.5, with no definite trend from bass to treble. This simple model has been already briefly discussed in Sec. 2.2.2 as an example of non-linear lumped element.

More realistic models have to take into account hysteretic properties of the hammer material. In the case of a piano hammer, it is known that the force-compression characteristic exhibits a hysteretic behavior, such that loading and unloading of the hammer felt are not alike. In particular, the dynamic force-compression characteristics is strongly dependence on the hammer normal velocity before collision. In order to account for these phenomena, Stulov [133] proposed an improved model where the contact force possesses history-dependent properties. The idea, which is taken from the general theory of mechanics of solids, is that the spring stiffness k in Eq. (5.1) has to be replaced by a time-dependent operator. Thus the contact force takes the form

$$f(x(t), t) = \begin{cases} -k[1 - h_r(t)] * [x(t)^\alpha], & x > 0, \\ 0, & x \leq 0, \end{cases} \quad (5.2)$$

where $h_r(t) = \frac{\epsilon}{\tau} e^{-t/\tau}$ is a *relaxation function* that controls the “memory” of the material. By rewriting the convolution explicitly, the Stulov force is seen to be:

$$f(x(t), t) = -kx(t)^\alpha + \frac{\epsilon}{\tau} e^{-t/\tau} \int_0^t e^{\xi/\tau} x(\xi)^\alpha d\xi, \quad \text{for } x > 0. \quad (5.3)$$

The Stulov model has proven to be successful in fitting experimental data where a hammer strikes a massive surface, and force, acceleration, displacement signal are recorded. Borin and De Poli [23] showed that it can be implemented numerically without significant losses in accuracy, stability and efficiency with respect to the simpler model (5.1). However, a recent study by Giordano and Mills [65] has investigated different experimental settings, where a hammer hits a vibrating string, and has showed that the Stulov model is not able to fit the data collected from such an experiment.

Useful results on contact models are also found from studies in robotics. Physical modeling of contact events is indeed an important aspect of dynamic simulations of robotic systems, when physical contact with the environment is required in order for

the system to execute its assigned task (for example, handling of parts by an industrial manipulator during assembly tasks, or manipulator collisions with unknown objects when operating in an unstructured environment). Marhefka and Orin [86] provide a detailed discussion of a collision model that was originally proposed by Hunt and Crossley [71]. Under the hypothesis that the contact surface is small, Hunt and Crossley proposed the following form for the contact force f :

$$f(x(t), \dot{x}(t)) = \begin{cases} -kx(t)^\alpha - \lambda x(t)^\alpha \cdot \dot{x}(t), & x > 0, \\ 0, & x \leq 0, \end{cases} \quad (5.4)$$

where variables and parameters are listed in Table 5.1. Similarly to Eqs. (5.1) and (5.2), the value of the exponent α depends only on the local geometry around the contact surface. In the following the value $\alpha = 2.8$ is chosen, which is close to values found in piano hammer felts. Note that the force model (5.4) includes both an elastic component kx^α and a dissipative term $\lambda x^\alpha \dot{x}$. Moreover, the dissipative term depends on both x and \dot{x} , and is zero for zero penetration.

Marhefka and Orin have studied the collision of a hammer onto a massive surface, which is assumed not to move during collision. When the two objects collide, the hammer initial conditions are given by $x_h = 0$ and $\dot{x}_h = v_{in}$ (the latter quantity meaning normal velocity before collision). Since the surface is assumed not to move, the hammer position x_h coincides with the penetration x , and the hammer trajectory is therefore described by the differential equation $m_h \ddot{x}_h = f(x_h, \dot{x}_h)$. Define the hammer velocity as $v = \dot{x}_h$, then it is shown in [86] that

$$\frac{dv}{dx_h} = \frac{\dot{v}}{\dot{x}_h} = \frac{(\Lambda v + K)x_h^\alpha}{v}, \quad \Rightarrow \quad \int \frac{v dv}{(\Lambda v + K)} = \int x_h^\alpha dx, \quad (5.5)$$

where two auxiliary parameters $\Lambda = -\lambda/m_h$ and $K = -k/m_h$ have been introduced for clarity. The integral in Eq. (5.5) can be computed explicitly and x_h can be written as a function of v :

$$x_h(v) = \left[\left(\frac{\alpha + 1}{\Lambda^2} \right) \left(\Lambda(v - v_{in}) - K \log \left| \frac{K + \Lambda v}{K + \Lambda v_{in}} \right| \right) \right]^{\frac{1}{\alpha+1}}. \quad (5.6)$$

Another remark by Marhefka and Orin is concerned with “stickiness” properties of the contact force f . From Eq. (5.4), it can be seen that f becomes inward (or sticky) if $v < v_{lim} := -1/\mu$. However, this limit velocity is never exceeded on a trajectory with initial conditions $x_h = 0$, $v = v_{in}$, as shown in the phase portrait of Fig. 5.1(a). The upper half of the plot depicts the trajectories of a hammer striking the surface with various positive normal velocities (trajectories are traveled in clockwise direction). Note that the negative velocities after collision v_{out} are always smaller in magnitude than the corresponding v_{in} . Moreover, for increasing v_{in} the resulting v_{out} converges to the limit value v_{lim} . The horizontal line $v = v_{lim}$ corresponds to the trajectory where the elastic and dissipative terms cancel, and therefore the hammer travels from right to left with

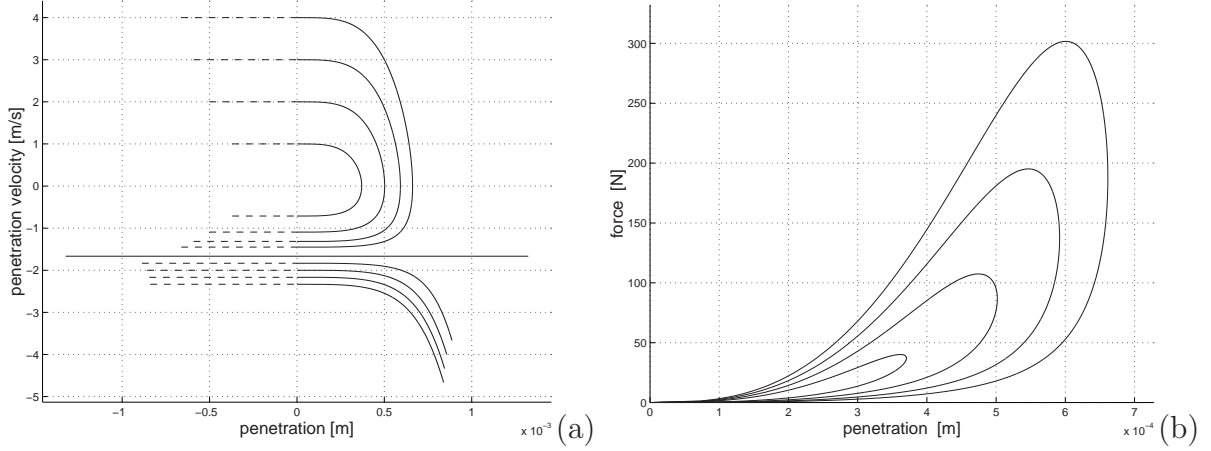


Figure 5.1: Collision of a hammer with a massive surface for various v_{in} 's; (a) phase portrait, (b) penetration-force characteristics. Values for the hammer parameters are $m_h = 10^{-2}$ [Kg], $k = 1.5 \cdot 10^{11}$ [N/m $^\alpha$], $\mu = 0.6$ [s/m], $\alpha = 2.8$, $v_{in} = 1 \dots 4$ [m/s].

constant velocity. This horizontal line separates two regions of the phase space, and the lower region is never entered by the upper paths. The lower trajectories are entered when the hammer is given an initial displacement $x_h < 0$ and initial *negative* velocity $v_{in} < v_{lim}$. If such conditions are imposed, then one of the lower trajectories is traveled from left to right: the hammer bounces back from the surface, while its velocity decreases in magnitude, due to the sticky force f .

Figure 5.1(b) shows the penetration-force characteristics during collision. Note that the dissipative term $\lambda x^\alpha \dot{x}$ introduces hysteresis. It can also be noticed that f never becomes zero for positive penetrations. This is a significant advantage with respect to the Stulov model [133].

5.1.2 Interaction with resonators

The contact force discussed in the last section can be used to excite a resonator model made of lumped mechanical elements such as masses springs and dampers.

The simplest possible oscillating system made of these three lumped elements is a second order oscillator of the form

$$\ddot{x}_o(t) + g_o \dot{x}_o(t) + \frac{k_o}{m_o} x_o(t) = -\frac{1}{m_o} f_{ext}(t), \quad (5.7)$$

where variables and parameters for the oscillator are given in Table 5.1, while f_{ext} is any external driving force. Such a one-dimensional model provides a basic description of the resonator in terms of its pitch $\omega_o = \sqrt{k_o/m_o}$ and quality factor $q_o = \omega_o/g_o$. However, in many cases this is a too poor description, since it cannot provide rich spectral contents. A slightly more sophisticated model is obtained by connecting N of the oscillators given

in Eq. (5.7) in parallel (i.e., the oscillators are driven by the same force; see Sec. 2.2 for a discussion of parallel and series connections). By choosing a different stiffness k_{ol} ($l = 1 \dots N$) for each oscillator, it is possible to account for a set $\{\omega_{ol}\}_{l=1}^N$ of partials of the resonator spectrum. The resulting structure is similar to that of Eq. (5.7). In matrix form, it can be written as

$$\begin{bmatrix} \ddot{x}_{o1}(t) \\ \vdots \\ \ddot{x}_{oN}(t) \end{bmatrix} + \mathbf{G}_o \begin{bmatrix} \dot{x}_{o1}(t) \\ \vdots \\ \dot{x}_{oN}(t) \end{bmatrix} + \mathbf{\Omega}_o^2 \begin{bmatrix} x_{o1}(t) \\ \vdots \\ x_{oN}(t) \end{bmatrix} = \mathbf{M}_o f_{ext}(t), \quad (5.8)$$

where the vector the matrices are given by

$$\mathbf{\Omega}_o = \begin{bmatrix} \omega_{o1} & & \mathbf{0} \\ & \ddots & \\ \mathbf{0} & & \omega_{oN} \end{bmatrix}, \quad \mathbf{G}_o = \frac{1}{q_o} \mathbf{\Omega}_o, \quad \mathbf{M}_o = \begin{bmatrix} 1/m_o \\ \vdots \\ 1/m_o \end{bmatrix}.$$

The structure given in Eq. (5.8) provides a high degree of controllability. The displacement and the velocity of the resonator are obtained as $x_o = \sum_{l=1}^N x_{ol}$ and $\dot{x}_o = \sum_{l=1}^N \dot{x}_{ol}$, respectively. The quality factor q_o controls the decay time of the resonator response. The frequencies $\{\omega_{ol}\}_{l=1}^N$ can be chosen to reproduce spectra corresponding to various geometries of one-, two- and three-dimensional resonators. In particular, it was shown by Fontana and Rocchesso [54, 105] that spherical, cubic and intermediate-shaped 3-D cavities can be modeled in an efficient and effective way. The first N resonances of a cavity can be mapped into the spring constants k_{ol} of the N oscillators, and morphing between different shapes can be obtained by designing appropriate trajectories for each of these resonances.

When this resonator is coupled with the contact model of Sec. 5.1.1, the external force f_{ext} in Eq. (5.8) is substituted by the contact force $f(x, \dot{x})$ given in Eq. (5.4). In this case the hammer penetration x is given by $x = x_h - \sum_{l=1}^N x_{ol}$. Note that by allowing the mass m_o to vary for each oscillator, the matrix \mathbf{M}_o can in principle be generalized to give control on the amounts of energy provided to each oscillator. This permits simulation of position-dependent interaction, in that different collision points excite the resonator modes in different ways. Early results about this generalized interaction were provided in [51].

The system is discretized using the bilinear transformation:

$$s = 2F_s \frac{1 - z^{-1}}{1 + z^{-1}}. \quad (5.9)$$

After this transformation, the resonator appears as a parallel filter bank of second-order bandpass filters, each one accounting for one specific mode of the resonator. Any bandpass filter can be accessed to its parameters of center-frequency and selectivity through the

physical quantities described above. The complete numerical system takes the form

$$\left\{ \begin{array}{l} \mathbf{x}_{ol}(n) = \bar{\mathbf{A}}_{ol}\mathbf{x}_{ol}(n-1) + \bar{\mathbf{b}}_{ol}[y(n) + y(n-1)], \quad (\text{for } l = 1 \dots N), \\ \mathbf{x}_h(n) = \bar{\mathbf{A}}_h\mathbf{x}_h(n-1) + \bar{\mathbf{b}}_h[y(n) + y(n-1)], \\ \mathbf{x}(n) = \mathbf{x}_h(n) - \sum_{l=1}^N \mathbf{x}_{ol}(n), \\ y(n) = f(\mathbf{x}(n)), \end{array} \right. \quad (5.10)$$

where

$$\begin{aligned} \mathbf{x}_{ol} &= \begin{bmatrix} x_{ol} \\ \dot{x}_{ol} \end{bmatrix}, \quad \mathbf{x}_h = \begin{bmatrix} x_h \\ \dot{x}_h \end{bmatrix}, \quad \mathbf{x} = \begin{bmatrix} x \\ \dot{x} \end{bmatrix}, \\ \bar{\mathbf{A}}_{ol} &= \frac{1}{\Delta_{ol}} \begin{bmatrix} \Delta_{ol} - 2k_{ol} & 4F_s m_o \\ -4k_{ol}F_s & 8F_s^2 m_o - \Delta_{ol} \end{bmatrix}, \quad \bar{\mathbf{A}}_h = \frac{1}{\Delta_h} \begin{bmatrix} \Delta_h & 4F_s m_h \\ 0 & \Delta_h \end{bmatrix}, \\ \bar{\mathbf{b}}_{ol} &= \frac{1}{\Delta_o} \begin{bmatrix} 1 \\ 2F_s \end{bmatrix}, \quad \bar{\mathbf{b}}_h = -\frac{1}{\Delta_h} \begin{bmatrix} 1 \\ 2F_s \end{bmatrix}, \end{aligned} \quad (5.11)$$

and where the quantities Δ_{ol} and Δ_h are given by $\Delta_{ol} = 4F_s^2 m_o + 2F_s m_o g_o + k_{ol}$ and $\Delta_h = 4F_s^2 m_h$, respectively. From Eqs. (5.10) it can be seen that the overall structure of the system resembles the block scheme depicted in Fig. 2.11. In particular, at each time step n the variables $\mathbf{x}(n)$ and $y(n)$ have instantaneous mutual dependence. This non-computable loop is solved with the K method as described in Sec. 2.3.2: the vector $\mathbf{x}(n)$ can be written as

$$\mathbf{x}(n) = \tilde{\mathbf{x}}(n) + \mathbf{K}f(n), \quad (5.12)$$

where

$$\mathbf{K} = -\left(\frac{1}{\Delta_h} + \frac{1}{\sum_{l=1}^N \Delta_{ol}} \right) \begin{bmatrix} 1 \\ 2F_s \end{bmatrix},$$

and $\tilde{\mathbf{x}}(n)$ is a computable vector (i.e. it is a linear combination of past values of the vectors \mathbf{x}_{ol} , \mathbf{x}_h and y). Substituting the expression (5.12) in the non-linear contact force equation (5.4), and applying the implicit function theorem, y can be found as a function of $\tilde{\mathbf{x}}$:

$$y = f(\tilde{\mathbf{x}} + \mathbf{K}y) \xrightarrow{\text{K method}} y = h(\tilde{\mathbf{x}}). \quad (5.13)$$

As described in Sec. 2.3.2, two choices are available for efficient numerical implementation of the K method. The first choice amounts to pre-computing the new non-linear function h off-line and storing it in a look-up table. Alternatively, h can be found iteratively at each time step from the vector $\tilde{\mathbf{x}}$, using the Newton-Raphson method. This latter approach is adopted here. The same approach was already taken in chapter 3 and

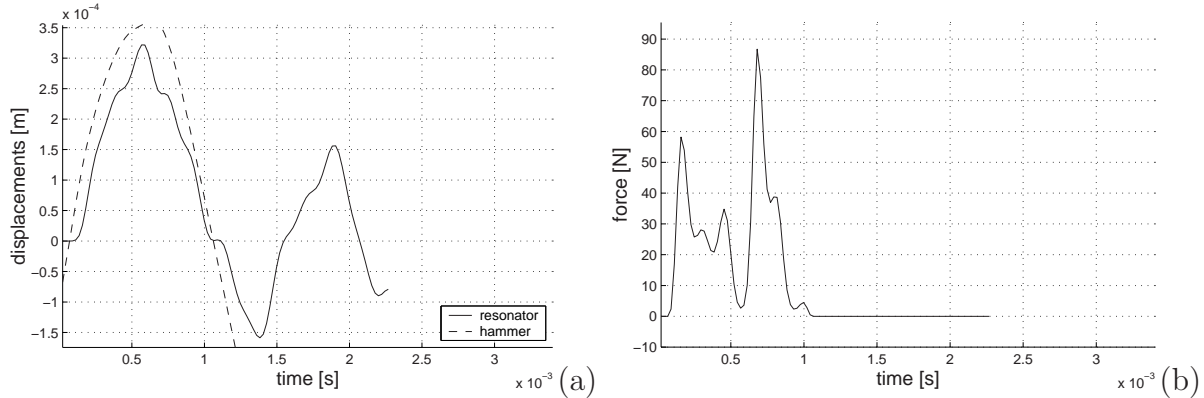


Figure 5.2: A transient attack from the model: (a) hammer and resonator displacements x_h and $\sum_{l=1}^N x_{ol}$; (b) contact force f during interaction. The resonator is given here $N = 3$ partials.

chapter 4 for dealing with non-linearities in a single reed model and in a model of the glottis, respectively.

Since most of the computational load in the numerical system comes from the non-linear function evaluation, the speed of convergence (i.e. the number of iterations) of the Newton-Raphson algorithm has a major role in determining efficiency of the simulations. In order to develop a real-time model, it is essential that the number of iterations remains small in a large region of the parameter space. To this end, analysis on the simulations has to be performed, where both the hammer and the resonator parameters are varied over a large range. Such analysis shows that in every conditions the algorithm exhibits a high speed of convergence. More precisely, the number of iterations is observed to be never higher than four, even when the Newton-Raphson algorithm is given extremely low tolerance errors ($\sim 10^{-13}$). Figure 5.2 displays an example of an attack transient, as obtained from the numerical model. The spikes in the force signal are due to the oscillations of the resonator partials during the collision.

5.2 Contact time: theory and simulations

The contact time t_0 (i.e. the time after which the hammer separates from the struck object) has a major role in defining the spectral characteristics of the initial transient. Qualitatively, a short t_0 corresponds to an impulse-like transient with a rich spectrum, and thus provides a bright attack. Similarly, a long t_0 corresponds to a smoother transient with little energy in the high frequency region. Therefore t_0 influences the spectral centroid of the attack transient.

It is known that the spectral content of the attack transient determines to a large extent the perceived quality of the impact. In a study on perceived mallet hardness, Freed [55], selected four acoustical parameters and studied their perceptual relevance through

listening tests. In his work, the acoustic stimuli were obtained from real recorded sounds of collision events, with mallets with varying hardness hitting various resonators. For each sound the subjects had to judge the perceived mallet hardness. It was found that the perception of hardness is strongly correlated to the spectral centroid of the attack transient. As already remarked, this latter parameter is in turn related to the contact time.

This section studies t_0 both analytically and experimentally (i.e. using numerical simulations). In Sec. 5.2.1, an equation is derived which relates t_0 to the physical parameters of the model, while Sec. 5.2.2 compares such analytical result to those obtained from simulations.

5.2.1 Analytical results

Using the contact model (5.4), Hunt and Crossley [71] studied the collision of a hammer with a rigid surface. They found an expression for the normal velocity after collision v_{out} in the limit of small μ (an analogous discussion is also reported in [86]). In this limit, v_{out} has a simple dependence on the normal velocity before collision, through a *coefficient of restitution* which in turns depends only on the hammer viscoelastic characteristics μ . When turning to the general case (i.e., when the parameter μ is allowed to take non-small values), studying the behavior of v_{out} is less trivial, and Hunt and Crossley do not address this case.

First of all, v_{in} and v_{out} correspond to the points where $x_h = 0$, i.e. to the roots of the right-hand side in Eq. (5.6). Therefore, from Eq. (5.6) v_{out} is found as

$$\begin{aligned} x_h(v_{out}) &= \Lambda(v_{out} - v_{in}) - K \log \left| \frac{K + \Lambda v_{out}}{K + \Lambda v_{in}} \right| = 0, \\ \Rightarrow \frac{e^{\mu v_{out}}}{1 + \mu v_{out}} &= \frac{e^{\mu v_{in}}}{1 + \mu v_{in}}. \end{aligned} \quad (5.14)$$

A first result is already evident from this equation: v_{out} depends only on the viscoelastic characteristics μ , and the input velocity v_{in} . There is no dependence on the spring stiffness k , the hammer mass m_h , the non-linear exponent α . A graphic study of the dependence of v_{out} on v_{in} and μ can be performed by plotting the function $\exp(\mu v)/(1 + \mu v)$, as in Fig. 5.3(a). It is seen that $v_{out} \rightarrow v_{lim}$ when v_{in} takes large values. This is consistent with the phase portrait in Fig. 5.1.

The second Eq. (5.14) can be rewritten as

$$e^{\mu v_{out}} = a(1 + \mu v_{out}), \quad \text{where} \quad a = \frac{e^{\mu v_{in}}}{1 + \mu v_{in}}. \quad (5.15)$$

Therefore v_{out} is the intersection of the exponential on the left-hand side and the linear function on the right-hand side, as shown in Fig. 5.3(b). The velocity v_{out} can be found numerically as the root of Eq. (5.15).

Having v_{out} , the contact time t_0 can now be computed. If collision occurs at $t = 0$, then the contact time is by definition given by $t_0 = \int_0^{t_0} dt$. Moreover, since $dt = dx_h/v$,

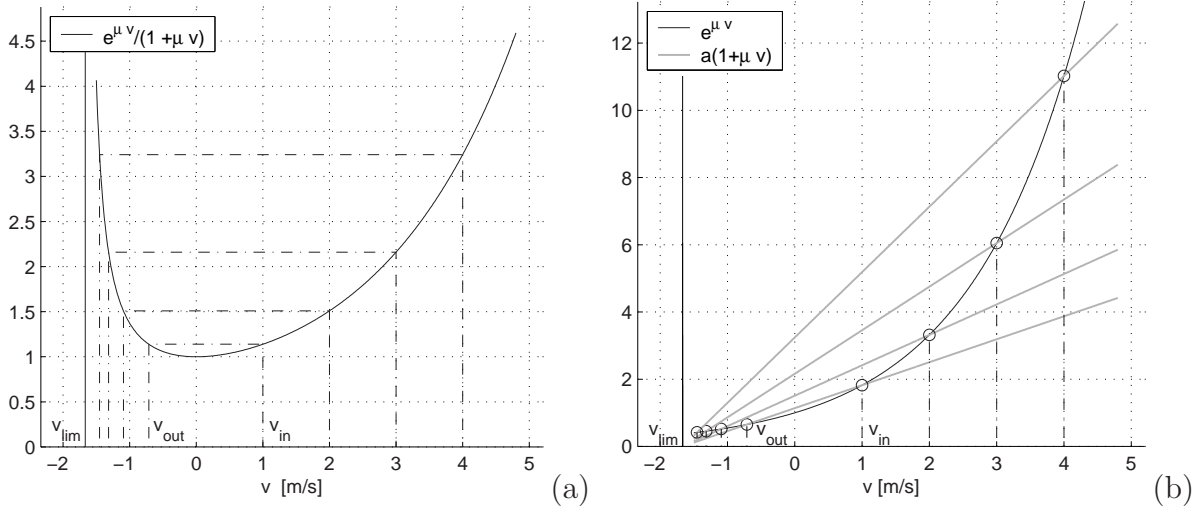


Figure 5.3: Graphic study of v_{out} for various v_{in} 's. Values for the parameters are the same used in Fig. 5.1.

also by definition, it is easily seen from Eq. (5.5) that

$$dt = \frac{dx_h}{v} = \frac{dv}{(\Lambda v + K)x_h^\alpha},$$

from which

$$t_0 = \int_0^{t_0} dt = \int_{v_{in}}^{v_{out}} \frac{dv}{(\Lambda v + K)x_h^\alpha}. \quad (5.16)$$

Recalling Eq. (5.6), x^α can be rewritten in the integral as a function of the velocity v . Thus, the integrand function depends only on v . Then straightforward calculations lead to the expression

$$t_0 = \left(\frac{\alpha + 1}{\Lambda^2}\right)^{-\frac{\alpha}{\alpha+1}} \cdot \int_{v_{in}}^{v_{out}} \frac{dv}{(\Lambda v + K) \left[\Lambda(v - v_{in}) - K \log \left| \frac{K + \Lambda v}{K + \Lambda v_{in}} \right| \right]^{\frac{\alpha}{\alpha+1}}}.$$

A more useful expression is obtained by substituting the parameter $\mu = \Lambda/K$ in this equation. In this way, t_0 can be computed as a function of the parameter set (m, k, μ, α) , together with the normal velocities before/after collision, (v_{in}, v_{out}) . Again, few calculation steps yield

$$t_0 = \left(\frac{m_h}{k}\right)^{\frac{1}{\alpha+1}} \cdot \left(\frac{\mu^2}{\alpha + 1}\right)^{\frac{\alpha}{\alpha+1}} \cdot \int_{v_{out}}^{v_{in}} \frac{dv}{(1 + \mu v) \left[-\mu(v - v_{in}) + \log \left| \frac{1 + \mu v}{1 + \mu v_{in}} \right| \right]^{\frac{\alpha}{\alpha+1}}}. \quad (5.17)$$

It can be checked that the constant outside the integral has dimension $[\text{s}^2/\text{m}]$, while the integral itself is a velocity $[\text{m}/\text{s}]$. Therefore, the whole expression on the right-hand side

has dimension [s]. Equation (5.17) states an important result: the contact time t_0 depends only on v_{in} and two parameters, i.e. the viscoelastic characteristic μ and the ratio m_h/k . A few remarks about Eq. (5.17):

- the integral has two singularities at the boundaries v_{out} and v_{in} . However, it can be checked that at these boundaries the integrand function converges asymptotically to $1/(v - v_{out})^{\alpha/(\alpha+1)}$ and $1/(v - v_{in})^{\alpha/(\alpha+1)}$, respectively. Therefore the integral always takes finite values;
- the integral depends only on v_{in} and μ . This is a consequence of Eq. (5.15), which states that v_{out} depends only on μ and v_{in} ;
- the constant outside the integral depends only on μ and the ratio m_h/k . Since neither m_h nor k affect the value of the integral, it follows that the power-law dependence $t_0(m_h/k) \sim (m_h/k)^{1/(\alpha+1)}$ holds;
- the dependence $t_0(\mu)$ is less easily established analytically; however, numerical integration of Eq. (5.17) can be used in order to study such dependence. Note that the singularities at v_{out}, v_{in} require additional care while integrating near the boundaries.

The results presented in this section emphasize a second advantage in using the contact model (5.4) instead of the Stulov model [133]: the explicit dependence of the force f on the system state (x, \dot{x}) , as stated in Eq. (5.4), allows the analytical study resulting in Eq. (5.17). A similar analysis is not possible with the Stulov model. In this case, the only results about the contact time characteristics are obtained experimentally, from the numerical simulations.

5.2.2 Comparisons with simulations

This section analyzes experimentally the influence of the model parameters on the contact time. Following the work and the terminology by Giordano and Mills [65], two types of numerical experiments are analyzed in the rest of the section. In a first setup the hammer strikes a rigid surface and rebounds from it: note that this is the same setting used in Sec. 5.2.1 for deriving Eq. (5.17). In the following this is termed a “Type I” experiment. A second experimental setup involves collision between the non-linear hammer and the resonator described in Sec. 5.1.2; in the following, this is referred to as a “Type II” experiment.

The strategy adopted here amounts to run several simulations in which the parameters m_h/k and μ are varied over a large range. Automatic analysis on these simulations computes the contact time t_0 and compares the obtained values with those resulting from numerical integration of Eq. (5.17). The analyzed simulations are run at a sampling rate $F_s = 44.1$ [kHz], and each simulation is $5 \cdot 10^{-2}$ [s] long. For Type II simulations, the resonator is given $N = 3$ partials.

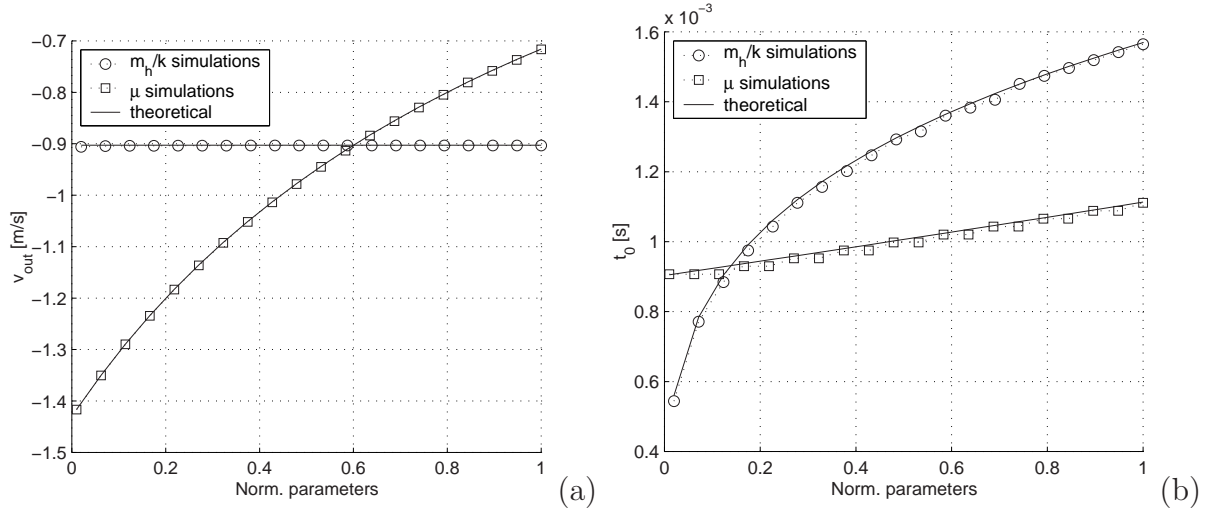


Figure 5.4: Dependence of (a) v_{out} and (b) t_0 on parameters m_h/k and μ for Type I simulations (solid lines computed from Eq. (5.17), discrete points obtained from simulations). The horizontal axes are in normalized coordinates, ranges for the two parameters are $m_h/k \in [6, 300] \cdot 10^{-12}$ [Kg m^α/N], $\mu \in [0.01, 1]$ [s/m]. Other parameters are as in Fig. 5.1.

Results for Type I experiments are summarized in Fig. 5.4, where both the theoretical behavior predicted by Eq. (5.17) and extracted data from numerical simulations are plotted. It can be seen that there is excellent accordance between theory and experiment. In particular, Fig. 5.4(a) shows that the values for v_{out} computed from the simulations do not depend on the ratio m_h/k , as predicted by Eq. (5.14). Moreover, from Fig. 5.4(b) it can be seen that the dependence $t_0(\mu)$ is almost linear in the observed range, and that the slope of this curve is small when compared to that of $t_0(m_h/k)$. In other words, the contact time t_0 is primarily affected by the value of m_h/k , and varies more slowly with respect to μ .

On the one hand, the accordance between the theoretical and the experimental t_0 values confirms the validity of the analytical study presented in Sec. 5.2.1. On the other hand, it assesses quantitatively the accuracy of the numerical implementation described in Sec. 5.1.2.

When analyzing Type II simulations, somewhat different results are found. This is due to the fact that in this case also the struck object is moving, therefore the contact time depends on both the hammer and the resonator parameters. In particular it is observed from Type II simulations that t_0 is always longer than in the Type I case, for any parameter setting.

Figure 5.5 plots the functions $t_0(\mu)$ and $t_0(m_h/k)$, for various resonator masses m_o . It can be noticed that the general dependence is always similar to that observed in Type I simulations. Moreover, the contact time is longer for light resonators and tends to the theoretical curve of Eq. (5.17) as m_o increases. This is an expected result, since Type I

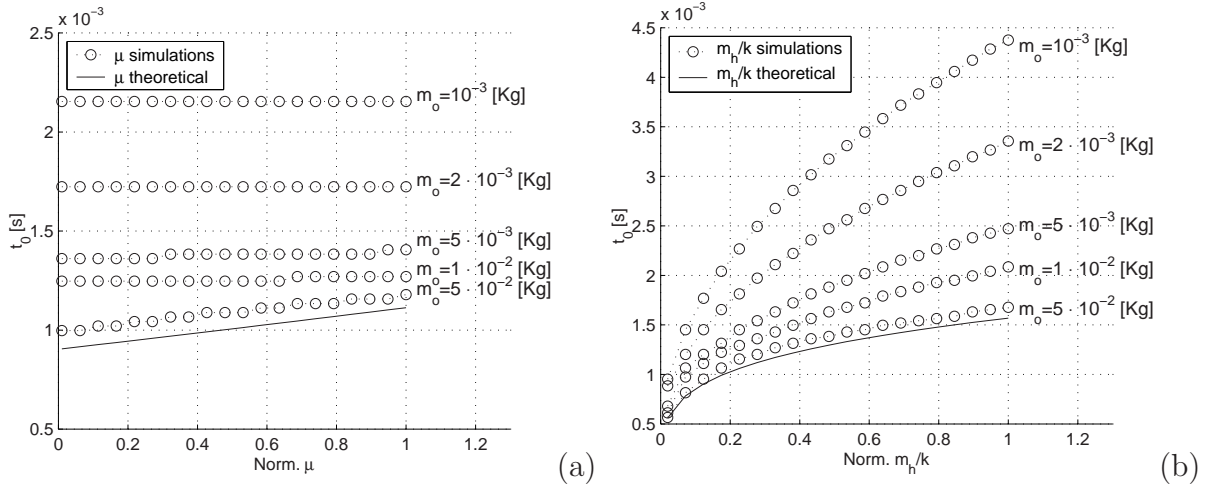


Figure 5.5: Dependence of t_0 on the parameters (a) μ and (b) m_h/k , for Type II experiments (solid lines computed from Eq. (5.17), discrete points obtained from numerical simulations). The horizontal axes are in normalized coordinates, with $\mu \in [0.01, 1]$ [s/m] and $m_h/k \in [6, 300] \cdot 10^{-12}$ [Kg m ^{α} /N]. Other parameters are as in Fig. 5.1.

simulations are equivalent to Type II simulations where the resonator mass m_o is given an infinite value.

The results outlined in this section, and in particular Eq. (5.17), can be regarded as complementary to the findings by Freed [55]. In his work, Freed studied experimentally the correlation between signal parameters (such as spectral centroid of the attack transient) and perceived hammer hardness, without any assumption on the physical description. Conversely, here it has been established a connection between signal parameters (namely t_0 , which is strongly correlated with spectral centroid) and an underlying physical model. Further study is needed in order to find a direct correlation between physical parameters and perceived hammer hardness.

5.3 Material perception

Rendering an impression of object material is not always cost effective –or even possible– in graphic rendering. On the other hand, physically-based sound models can give the possibility to embed material properties with almost no computational overhead. Section 5.3.1 discusses the acoustic cues exploited by the auditory system for the perception of material, and examines how these cues are controlled in the hammer-resonator model. Section 5.3.2 presents the results obtained from listening tests with synthetic stimuli.

5.3.1 Acoustic cues

At present, few studies have investigated what acoustic cues (if any) are exploited by the auditory system in order to recognize materials of sound sources. Based on theoretical considerations, Wildes and Richards [153] suggested the overall decay time as a significant cue, since it is a direct measure of internal friction in a given material. However, this is only true when a standard inelastic linear solid model is assumed.

Two recent studies with listening subjects provided some experimental basis to this conjecture, but results were not in accordance. Lutfi and Oh [84] found that changes in the decay time are not easily perceived by listeners, while changes in the fundamental frequency seem to be a more salient cue. On the other hand, Klatzky *et al.* [78] showed that decay plays a much larger role than pitch in affecting judgment. Both these studies made use of synthetic stimuli obtained using additive synthesis algorithms. Therefore, no realistic attack transients could be obtained.

Even less clear is how to embed material properties in physically-based sound synthesis algorithms, and how to control them by accessing the physical parameters of the sound models. Djoharian [38] showed that finite difference models of resonators can be covered by a “viscoelastic dress” to fit a given frequency-damping characteristic, which is taken as the sound signature of the material. This approach relies on a low-level physical description and, as a result, very accurate yet computationally expensive algorithms are obtained. The sound examples provided by Djoharian convinced many researchers of the importance and the effectiveness of materials in sound communication. No impact model was used in this study. Therefore the sounds are impulse responses with no physical attack transients.

This section investigates the use of the contact model presented in Sec. 5.1 for conveying material perception to the listener. Using such an accurate yet efficient physical model for subjective tests is advantageous over using damped sinusoids or other signal-based sound models, in that realistic interactions can be reproduced. As a result, complex and realistic attack transients can be kept in the stimuli, thus eliminating possible biases due to oversimplified test sounds.

The results presented in the next section are based on a listening test in which experimental subjects are asked to listen to acoustic stimuli synthesized using the hammer-resonator model. When designing the acoustic stimuli for the test, it has to be considered that the contact sound produced by hammer-resonator interaction can give information on both the hammer and the resonator properties. This perceptual effect is known as *phenomenical scission* in experimental psychology. As an example, Freed [55] showed that not only properties of the resonator but also the hammer hardness (see Sec. 5.2) can be perceived from percussive sounds.

Since the perception of material relates to the properties of the resonator, the acoustic stimuli for the test have to be synthesized using the same hammer, i.e. the same set of coefficients m_h, k, μ, α . The impact velocity v_{in} of the hammer has to be fixed as well. In this way, a constant excitation is provided to the resonator. The resonator is constructed from Eq. (5.8). For the actual stimuli, the value $N = 1$ is chosen.

The choice of using only one partial is justified by the fact that previous studies [153, 84, 78] have concentrated exclusively on two acoustic parameters of the stimuli, namely pitch and decay time. Therefore, a single second-order oscillator is enough for controlling these two parameters: pitch is defined using the center frequency $\omega_o = \sqrt{k_o/m_o}$ of the oscillator, while decay characteristics are controlled through the quality factor q_o . More precisely, it is known that for a second-order oscillator q_o relates to decay via the equation $q_o = \omega_o t_e / 2$, where t_e is defined as the time for the sound to decay by a proportion $1/e$.

The stimuli used in the test described in the next section are a set of 100 sounds. These are obtained using five equally log-spaced pitches from 1000 to 2000 [Hz], together with 20 equally log-spaced quality factors from 5 to 5000. These extremal q_o values correspond to typical values found in rubber and aluminium, respectively. In a recent study on plucked string sounds, Tolonen and Järveläinen [137] found that relatively large deviations (between -25% and $+40\%$) in the decay time are not perceived by listeners. With the values that have been chosen here, the relative lower/upper spacing between q_o values is $-31\%/+44\%$.

The mapping from the two acoustic parameters and the physical parameters of the resonator is chosen as follows:

- the stiffness k_o is given a fixed value for all the stimuli, so that for each ω_o the corresponding mass is computed as $m_o = k_o/\omega_o^2$.
- For each quality factor q_o , the corresponding damping coefficient is computed as $g_o = \omega_o/q_o$.

5.3.2 Experimental results

The results presented in this section are based on a listening test with 22 experimental subjects. The subjects had to listen to the 100 sounds described in the previous section, and to indicate what material each sound was coming from, choosing from a set of four material classes: rubber, wood, glass and steel (this approach is analogous to that adopted in [78]). Each sound was played once and followed by a pause in which subjects had to choose the corresponding material class. All of the 22 listeners were volunteers, both expert and non-expert listeners, all reported normal hearing.

Figure 5.6 summarizes results of the experiment: it shows the proportion of subjects who assigned each sound to a given material category, as a function of the two acoustic cues (pitch and quality factor). The intersubject agreements (proximity of the response proportions to 0 or 1) are qualitatively consistent with indications given by Wildes and Richards [153], namely

- The responses tend to cluster in horizontal stripes. This result suggests that the quality factor q_o is the most significant cue, while the listeners' choices are less affected by the pitch ω_o .

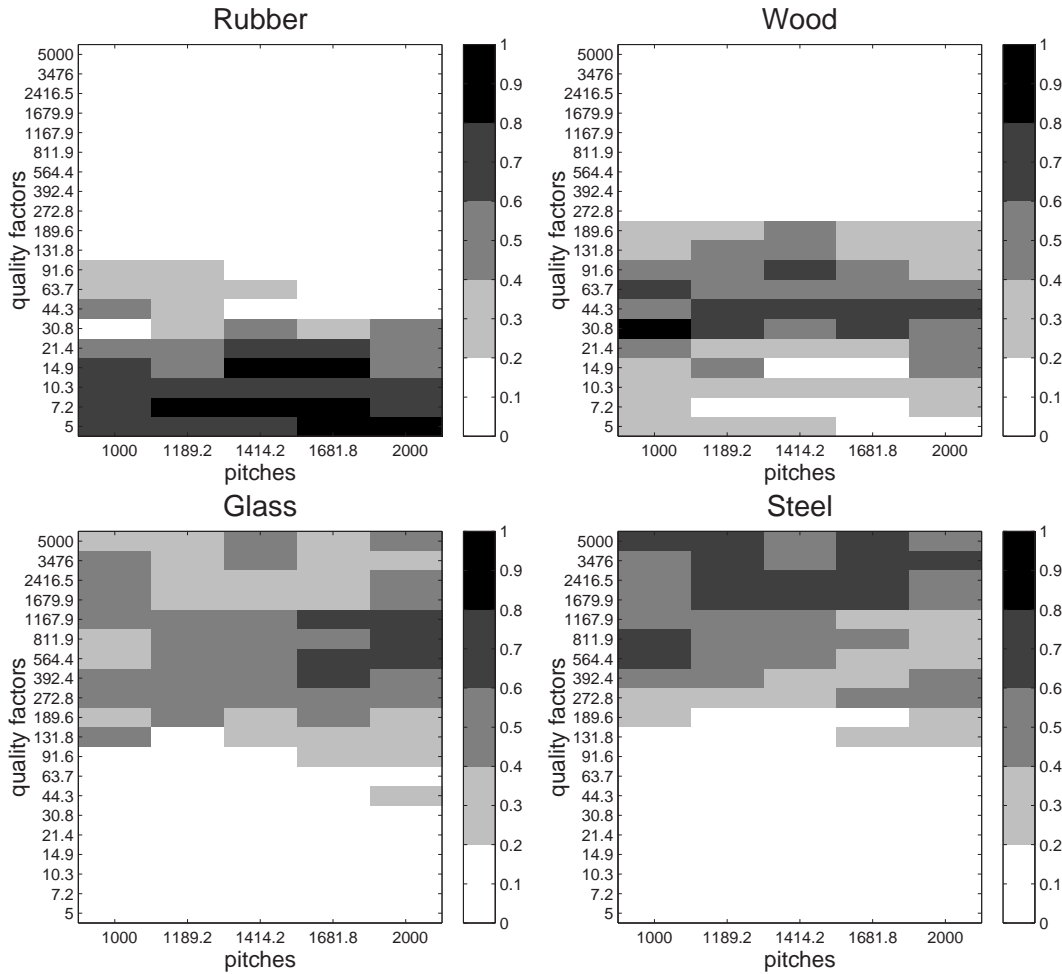


Figure 5.6: *Proportion of subjects who recognized a certain material for each sound example. Pitches (in [Hz]) and quality factors are on the horizontal and vertical axes, respectively.*

- The quality factor q_o (and therefore the decay time t_e) is in increasing order for rubber, wood, glass and steel.

A slight dependence on pitch can be noticed: rubber and glass tend to be preferred at high pitches, while wood and steel are more often chosen at low pitches. Klatzky *et al.* [78] found a similar trend for glass and steel, while they observed the opposite for rubber and wood (i.e. these two materials were preferably chosen at low and high pitches, respectively). However, the findings in [78] are not easily comparable to those illustrated in Fig. 5.6, since a different pitch range was chosen in [78] (namely, five equally log-spaced frequencies from 100 to 1000 [Hz]).

Table 5.2 collects the q_o ranges for each material. The boundaries of these ranges are found by computing the minimum and maximum values where more than 50% of the

<i>Material</i>	q_o	t_e [s]
<i>Rubber</i>	[5, 44.3]	$[8 \cdot 10^{-4}, 1.41 \cdot 10^{-2}]$
<i>Wood</i>	[14.9, 131.8]	$[2.3 \cdot 10^{-3}, 3.53 \cdot 10^{-2}]$
<i>Glass</i>	[189.6, 5000]	$[4.34 \cdot 10^{-2}, 1.1254]$
<i>Steel</i>	[272.8, 5000]	$[4.34 \cdot 10^{-2}, 1.5915]$

Table 5.2: *Minimum and maximum values of the quality factor and the decay time for which more than 50% of the experimental subjects have chosen a given material.*

subjects chose one of the four materials. The corresponding ranges for the decay time t_e are also given.

From both Fig. 5.6 and Table 5.2, it appears that the upper and lower halves of the q_o range are well separated, while materials within each of these two regions are less easily discriminated. In particular, it is evident from the figure that the regions corresponding to glass and steel are largely overlapping, while ranges for rubber and wood are better delimited. After the test, many subjects reported that the indication “glass” was not immediately clear to them, since they could not guess what sound is produced by a bar made of glass.

Another possible explanation for the worse performance in the high q_o -range has to do with the synthesis model: for long decay times (such as those of glass and steel) a single partial with exponential decay envelope is probably a too poor approximation of reality, and a more accurate description is needed. Figure 5.7 plots the same data as in Table 5.2 on the $q_o/\omega_o, t_e$ plane, thus allowing direct comparison with the qualitative plot reported by Wildes and Richards [153]. Again, the separation between the low and high q_o -ranges appears clearly. Rubber and wood are better discriminated, while the ranges for glass and steel are largely overlapping.

These findings show that decay (or quality factor q_o) plays a much larger role than pitch ω_o in material perception. Moreover, material classification by subjects is qualitatively in accordance with reported measures of internal friction coefficients for these material classes. This indicates that even the extremely simple resonator model (5.8) with $N = 1$ can elicit perception of material, provided that it allows for control over the salient acoustical cues. When using a higher number N of partials, more realistic and less “cartoonized” sounds are obtained while control over material perception is maintained through the parameter q_o .

However, measures on the intersubject agreement show that the classification is inaccurate for high quality factors (glass and steel), thus suggesting that the overall decay time does not fully account for material properties and that control on the decay shape of

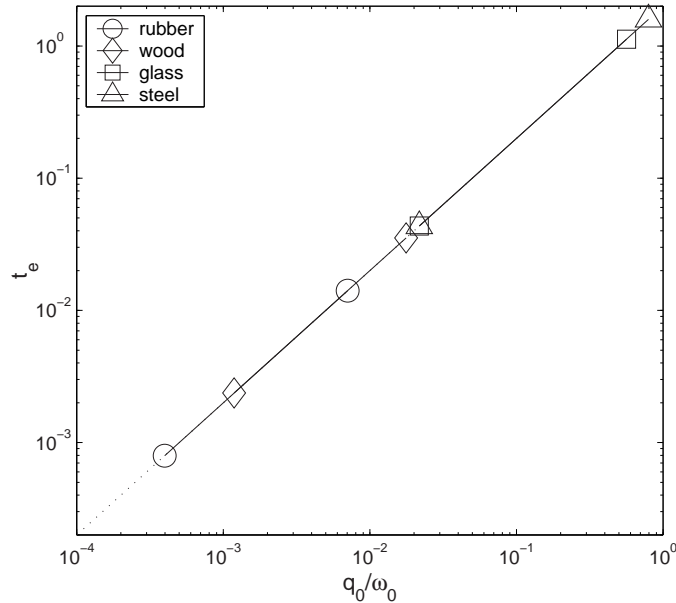


Figure 5.7: *Distribution of materials on the $q_0/\omega_0, t_e$ plane.*

each partial would be needed in order to allow for a more accurate description of reality. Analysis and subjective experiments with real sounds have to be performed, in order to understand how the classification is improved and to investigate whether decay shape can play a role in helping material perception. This information can then be exploited to develop an improved resonator model. Preliminary observations [149] suggest that experiments with real sounds yield perceptual results that are qualitatively similar to those summarized in Fig. 5.6.

Summary

A hammer-resonator model has been developed, and compared to existing contact models in the literature. In particular, it has been shown that the proposed contact model has common features with the piano hammer felt model proposed by Stulov. However, further research is needed to compare the two, and to discuss the possible use of the model in physically-based synthesis of the piano.

In Sec. 5.1 it has been shown that an accurate and efficient numerical implementation of the model can be obtained by using the bilinear transform in combination with the K method. The resulting numerical algorithm can be easily implemented in real-time on general-purpose hardware.

Section 5.2 has discussed the properties of the contact force, focusing on the influence of physical parameters in perceptual features of the interaction. Contact time has been investigated in detail, since this parameter affects the spectral centroid of the transient

attack and influences the perceived quality of the collision. Further research and psychophysical experiments are needed in order to validate the ability of the model to convey perception of impact hardness.

Section 5.3 has focused on the resonator properties, and has explored the ability of the model to elicit perception of the resonator material to the listener. First, it has been shown that the physical parameters give control over the salient acoustic cues. Second, listening tests with synthetic stimuli obtained from the model have provided perceptual validation of the model. Results from the tests have been compared to the existing literature.

